International Forum on Aeroelasticity and Structural Dynamics
IFASD 2024
17-21 June 2024, The Hague, The Netherlands

NONLINEAR AEROELASTICITY CHARACTERISTICS AND DYNAMICS RESPONSE ANALYSIS OF UNMANNED MULTI-BODY AIRCRAFT

Zhu Zijian[1], Bi Ying[2]*, Zhu Chen[3], Ying Zhuolin[4], Zhang Jian[5]

[1, *] Institute of Engineering Thermophysics, Chinese Academy of Sciences, Beijing, 100190, China;

[2] School of Aeronautics and Astronautics, University of Chinese Academy of Sciences, Beijing, 100049, China;

[3] National Key Laboratory of Science and Technology on Advanced Light-Duty Gas-Turbine, Beijing, 100049, China;

[4] Key Laboratory of UAV Emergency, Rescue Technology, Ministry of Emergency Management, Beijing, 102202, China

Keywords: multi-body aircraft, aeroelastic, modal reduction, Geometric nonlinearity

Abstract: The Unmanned multi-body aircraft (MBA) presents significant advantages for enhancing aspect ratio, optimizing aerodynamic performance, and reducing the challenges associated with takeoff and landing. Despite its potential, current research on this configuration predominantly addresses the rigid body aspect, entirely overlooking the geometric nonlinearity arising from aeroelastic deformation during flight. This study investigates the MBA configuration by employing the substructure method and modal reduction techniques to develop a reduced-order nonlinear structural model. Subsequently, the surface dipole lattice method is utilized to formulate the nonlinear aerodynamic model. By coupling the explicit nonlinear structural equations with the explicit aerodynamic equations via Lagrange equations, we derive an explicit dynamic representation of a high-dimensional aeroelastic system encompassing both geometric and concentrated nonlinear factors. Based on the established aeroelastic system equations, we perform a parametric analysis and mechanistic study of flutter characteristics. The results reveal that the flutter speed of the MBA configuration decreases as the number of modular aircraft increases. Additionally, nonlinear factors significantly influence the flutter characteristics across various configurations and cannot be disregarded.

1 INTRODUCTION

The increasing demand for near-space applications has significantly focused the aerospace community's attention on high-altitude long-endurance (HALE) unmanned aerial vehicles (UAVs)

[1,2]. Given the stringent requirements for lightweight structures and high endurance in near-space operations, high aspect ratio configurations have become essential for these aircraft. Although such designs offer superior aerodynamic characteristics, they also impose stricter requirements on takeoff and landing environments, transportation conditions, and structural integrity. These challenges are particularly pronounced in the relatively harsh low-altitude flight conditions, where the flexible structures of HALE UAVs are prone to undesirable aeroelastic phenomena [3,4].

In this context, the concept of modular UAVs has emerged. Independent flying units sequentially take off and achieve wingtip docking in the relatively stable stratosphere through mechanisms such as hinges. This configuration not only offers excellent aerodynamic characteristics but also effectively mitigates challenges related to limited takeoff and landing sites and the complexities of low-altitude flight [5].

The initial concept of modular UAVs dates back to the mid-20th century. Under the guidance of Dr. Vogt, two lightweight aircraft and a small transport aircraft achieved wingtip docking using ropes [6]. Over the next half-century, various countries conducted similar experiments. However, these efforts did not yield the desired outcomes due to incomplete theoretical frameworks and technological gaps [6,7]. Recently, with the exploration of near-space, the modular configuration has regained attention. At the beginning of this century, the McGill team compared the aerodynamic parameters of modular aircraft flight and formation flight, addressing the challenges of high maneuverability in military operations and long-distance air transport, and highlighting the importance of modular aircraft transport systems [6]. Patterson described a modular configuration where a mother ship handles transportation while sub-aircraft perform missions [8]. The Wlach team proposed a wingtip connection concept to enhance flexibility.

Systematic research in this area has gained momentum over the past decade. Montalvo and colleagues introduced the concept of meta-aircraft, achieving wingtip docking through magnetic connections. They modeled the dynamics of these connections, considering factors such as sensor errors, atmospheric disturbances, and contact loads during docking events, and analyzed the fault tolerance of the connection behavior [9]. In subsequent years, Montalvo's team conducted studies on the flight dynamics, control, and stability of modular aircraft, further validating the controllability and feasibility of the wingtip connection configuration [10,11]. Similarly, the Cooper team demonstrated the feasibility of wingtip docking by developing dynamic models and control architectures for the aircraft system, enabling in-flight wingtip docking [12]. Both teams utilized a spring-damper magnet system to simulate the dynamics at the connection points. Subsequent studies included real-world experimental simulations focusing on control systems and near-field aerodynamic effects [12-14]. However, the spring-damper magnet system is not the sole method for modeling connection points; hinge structures also represent a viable approach for achieving wingtip connections [15]. Hinge mechanisms, allowing only relative roll motion between aircraft, are inherently unstable and require the design of appropriate control strategies [16]. The Alexander team also conducted research on flight dynamics, the dynamic process of connection behavior, and controllability for this configuration [17-19].

In summary, the analysis of feasibility and controllability remains the primary research focus for modular configurations. Building on this foundation, dynamic analysis of the connection process and subsequent flight dynamics and stability analysis are progressing. However, research on the aeroelastic characteristics of this configuration is still in its infancy. As a type of high aspect ratio

aircraft, the inherent geometric nonlinearity and aeroelastic issues arising from its high flexibility warrant significant attention[20]. In the field of nonlinear aeroelasticity, current methods primarily employ linearization or equivalent linearization techniques for local dynamic analysis, focusing on stability issues brought about by nonlinear factors [20,21]. Addressing such high-dimensional nonlinear systems necessitates the development of reduced-order aeroelastic system models that balance accuracy and efficiency, achieving higher numerical stability with fewer degrees of freedom [21-23].

2 METHODOLOGIES

2.1 Geometric nonlinear elasticity

In the presence of aerodynamic loads, the wings of highly flexible aircraft exhibit minimal strain, maintaining adherence to linear elasticity theory within the structural material. However, notable nonlinear large deformations emerge, rendering the small deformation assumption invalid. In such scenarios, it becomes imperative to incorporate the second-order terms of deflection derivatives into the geometrically nonlinear elastic equations.

To tackle this challenge, the Updated Lagrange method is employed for formulating the matrix equations of the elements [24].

$$({}^{t}\mathbf{K}_{L} + {}^{t}\mathbf{K}_{NL})\mathbf{u} = {}^{t+\Delta t}\bar{\mathbf{Q}} - {}^{t}\mathbf{F} \tag{2.1}$$

The corresponding dynamic equations are:

$${}^{t}\mathbf{M}\,{}^{t+\Delta t}\ddot{\mathbf{u}} + ({}^{t}\mathbf{K}_{L} + {}^{t}\mathbf{K}_{NL})\mathbf{u} = {}^{t+\Delta t}\bar{\mathbf{Q}} - {}^{t}\mathbf{F} \tag{2.2}$$

In many dynamic problems, it can still be assumed that the structure undergoes small amplitude vibrations around its static equilibrium state, including issues related to dynamic stability. This can be denoted as

$$\mathbf{u} = \bar{\mathbf{u}} + \mathbf{x} \tag{2.3}$$

Here, $\bar{u}$ represents the static equilibrium large deformation obtained from the equation; x denotes the small amplitude vibration displacement. Based on the equations and the static equilibrium conditions, the free vibration equation of the system under steady loads can be expressed as:

$$\mathbf{M}_{T}\ddot{\mathbf{x}} + \mathbf{K}_{T}\mathbf{x} = 0 \tag{2.4}$$

2.2 Non-planar Dipole Panel Method

Considering that the design state of the aircraft should avoid large oscillations and stall phenomena, it is still feasible to establish the aerodynamic calculation method for the wing's large deformation based on the small perturbation potential flow theory of Euler equations. Therefore, this paper employs the surface dipole lattice method for aerodynamic modeling of a high aspect ratio flying wing UAV layout.

The dipole lattice method first requires a reasonable aerodynamic mesh division of the lifting surface. Traditional linear aeroelastic analysis involves meshing only on the planar lifting surface, resulting in the generalized unsteady aerodynamic expression as:

$$\boldsymbol{Q}^{*}=\frac{1}{2}\rho V^{2}\boldsymbol{A}\boldsymbol{q} \tag{2.5}$$

Here, A_{ij} is the generalized aerodynamic influence coefficient matrix.

$$\boldsymbol{A}=\phi_{P}^{T}\boldsymbol{S}\boldsymbol{D}^{-1}(\frac{\partial\phi_{H}}{\partial x}+i\frac{k}{b}\phi_{H}) \tag{2.6}$$

where D represents the unsteady aerodynamic influence coefficients. ϕ_H is the modal matrix at the control points; k is the reduced frequency, and b is the reference length. ϕ_P is the modal matrix at the aerodynamic grid points. $S=diag\left(\Delta S_1,\cdots,\Delta S_n\right)$ is the area-weighted matrix, with diagonal elements representing the areas of each aerodynamic grid.

The aforementioned traditional dipole calculation method requires modification to accurately account for unsteady aerodynamics on surfaces experiencing large deformations. To address this, we must correct for non-coplanar aerodynamic forces. This involves initially generating a three-dimensional mesh on the curved lifting surface, which is continuously updated to follow structural deformations, as illustrated in Figure 1, depicting the surface dipole lattice division. In this configuration, the dipole lines are arranged on a spatial curved surface, and the dipole grid becomes a spatial grid. Furthermore, it is crucial to establish a local coordinate system to accurately represent the actual deformation of the wing in the airflow, $\cos\varphi_j$ is directly related to the shape of the lifting surface, including factors such as the sweep angle. The kernel function K_{ij} is also intricately linked to the wing's deformation.

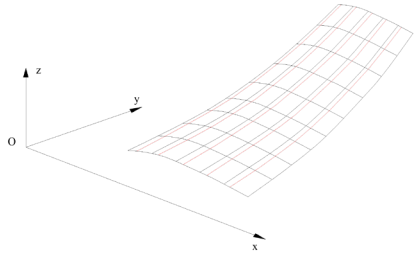

Figure 1. Curved surface dipole lattice division

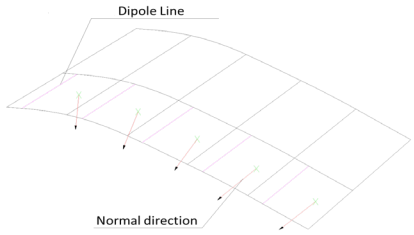

Figure 2: Dipole lines and normal direction

The specific expression of the kernel function is given as follows:

$$K=\lim_{n_i\to 0}\frac{\partial}{\partial n_i}\left\{e^{-i\omega\bar{x}/U_\infty}\int_{-\infty}^{\bar{x}}\frac{\partial}{\partial n_j}\left[\frac{1}{R'}\cdot e^{i\bar{\omega}\left(\lambda_1-M_\infty R'\right)/M_\infty}\right]d\lambda_1\right\} \tag{2.7}$$

Where $\left(x_i,y_i,z_i\right)$ is the receiving point, $\left(x_j,y_j,z_j\right)$ is the disturbance point, $\bar{x}=x_i-x_j$, $\bar{y}=y_i-y_j$, $\bar{z}=z_i-z_j$, n_i is the normal direction at point $\left(x_i,y_i,z_i\right)$ on the wing surface, n_j is the normal direction at point $\left(x_j,y_j,z_j\right)$ on the wing surface. In the non-coplanar lifting surface, n_i , n_j is an arbitrary vector in space, determined in the local coordinate system of each respective grid. $\frac{\partial}{\partial n_i}$,

$\frac{\partial}{\partial n_j}$ is related to the shape of the wing surface in space (curvature deformation, torsional deformation).

The key modification for surface dipole lattice lies in determining the boundary conditions. Surface dipole lattice requires computing the normal induction velocity (normal induced velocity) of the unit mesh to determine the boundary conditions. Traditional methods only focus on the vertical downwash velocity in the z-direction. The modes related to the boundary conditions also need modification. When introducing modes, the geometric deformation and structural dynamic characteristics of the highly deformed wing should be fully considered. Assuming the structure undergoes small amplitude vibrations around its equilibrium position of large static deformation, the concept of natural frequency and mode from linear system vibration theory can still be applied. This analysis is referred to as the "quasi-mode" method.

Due to the influence of large deformation, the wing cannot be approximated to move near the x-y plane. Therefore, the boundary conditions of the surface dipole method are fundamentally different from the simplified methods used in the flat plane scenario.

n represents the normal vector to the surface S(x, y, z) = 0, and (n, x), (n, y), (n, z) are the angles between the normal and the coordinate axes. Assuming the surface motion takes the form of $S = Se^{i\omega t}$, then the normal velocity of the object's motion is given by:

$$\left(U_n\right)_{\mathrm{b}} = \left(\frac{\partial x}{\partial t}\right)_{\mathrm{b}} \cos(\mathrm{n,x}) + \left(\frac{\partial y}{\partial t}\right)_{\mathrm{b}} \cos(\mathrm{n,y}) + \left(\frac{\partial z}{\partial t}\right)_{\mathrm{b}} \cos(\mathrm{n,z}) \tag{2.8}$$

The more general boundary conditions for the surface are obtained as:

$$\boldsymbol{w} = (i\frac{k}{b} f_H + \frac{\partial f_H}{\partial n})q \tag{2.9}$$

Where $\boldsymbol{w} = \boldsymbol{U}_n^b / V_\infty$ is the projection of the induced velocity of the grid on the normal vector, and f_H represents the normal modal vector at the control point after specific nonlinear static deformations of the wing, namely, the "quasi-mode" vector obtained based on geometric nonlinear effects. In the surface dipole lattice method, the modal vectors f_H already include information about the wing's nonlinear static deformations. Similar to the planar dipole lattice method, the aerodynamic calculation in the surface dipole lattice method can also be expressed as follows:

$$Q_f = \frac{1}{2}\rho V^2 A_f q \tag{2.10}$$

$$A_f = f_P^T S D_f^{-1} (\frac{\partial f_H}{\partial n} + i\frac{k}{b} f_H) \tag{2.11}$$

Where D_f is the spatial surface dipole influence coefficient matrix, and f_P is the "quasi-mode" vector at the aerodynamic action point after nonlinear static deformations of the wing. Solving the above equation yields the pressure difference on the curved lifting surface.

2.3 Interpolation methods for curved wing structures/aerodynamics

Due to the possibility of non-coincident nodes between the aerodynamic grid and the structural mesh, it is necessary to establish a spatial curved surface three-dimensional interpolation method to achieve coupling between aerodynamics and structure. This facilitates the establishment of a structural-aerodynamic coupling mechanism for static and dynamic aeroelastic analysis. Following this approach, traditional Thin Plate Splines (TPS) methods can be extended to multi-dimensional space, making them applicable for transferring motion parameters and load information across the structure/aerodynamic interface of highly deformed curved wing configurations.

Let $X_i = \left\{x_i^1, \cdots, x_i^N\right\}, (I = 1, 2, \cdots, n)$ be the N-dimensional vector in n given vectors, and its corresponding multi-dimensional function $W_i = \left\{w_i^1, \cdots, w_i^M\right\}, \left(i = 1, 2, \cdots, n\right)$, representing a vector in M-dimensional space. For each component of W, we establish the following interpolation function:

$$w^k(\mathbf{X}) = c_1^k + \sum_{p=1}^{N} c_{p+1}^k x_p + \sum_{i=1}^{n} c_{N+1+i}^k r_i^2 \ln(r_i^2 + \varepsilon) \tag{2.12}$$

Where $r_i^2 = \sum_{p=1}^{N}\left(x_p - x_{pi}\right)^2$ are the basis functions, and $c_1, c_2 \cdots c_{N+1+n}$ are the undetermined coefficients. For a general flat surface, $\varepsilon = 10^{-2} \sim 1$, and for surfaces with singularity, it can be chosen as $10^{-5} \sim 10^{-6}$. x_{pi} represents the p-th coordinate of the i-th node.

The undetermined coefficients are determined by the following system of equations:

$$\sum_{i=1}^{n} c_{N+1+i}^k = 0 \tag{2.13}$$

$$\sum_{i=1}^{n} c_{N+1+i}^k x_i^p = 0, \quad p = 1, 2, \cdots, N \tag{2.14}$$

$$c_1 + \sum_{p=1}^{N} c_{p+1} x_{pj} + \sum_{i=1}^{n} c_{N+1+i} r_{ji}^2 \ln(r_{ji}^2 + \varepsilon) + h_j c_{N+1+j} = W_j, \quad j = 1, 2, \cdots, n \quad , \quad i \neq j \tag{2.15}$$

In the equation above, $r_{ji}^2 = \sum_{p=1}^{N}\left(x_{pj} - x_{pi}\right)^2$, h_j represents the weighting coefficients corresponding to the j-th node, which are predetermined by the calculator. When all weighting coefficients are set to zero, the fitted curve, surface, or hypersurface precisely passes through all the function values of the nodes. When all weighting coefficients are set to a non-zero value, it exhibits the properties of the least squares method. When weighting coefficients take various values, it allows for approximation curves, surfaces, or hypersurfaces with different degrees of fitting.

Applying the interpolation theory mentioned above to the coupling of aeroelastic structures/aerodynamic interfaces allows for the transfer of motion information from the structural interface to the aerodynamic interface. Considering the three-dimensional nature of structural

configurations under large deformations, if the coordinates of n structural nodes are known as X_S and their deformation vectors as U_S, we need to obtain the deformation vectors U_A corresponding to m aerodynamic grid nodes at point X_A. Where:

$$X_S=\begin{bmatrix} x_{S1} & y_{S1} & z_{S1} \\ \vdots & \vdots & \vdots \\ x_{Sn} & y_{Sn} & z_{Sn} \end{bmatrix} U_S=\begin{bmatrix} u_{S1} & v_{S1} & w_{S1} \\ \vdots & \vdots & \vdots \\ u_{Sn} & v_{Sn} & w_{Sn} \end{bmatrix} X_A=\begin{bmatrix} x_{A1} & y_{A1} & z_{A1} \\ \vdots & \vdots & \vdots \\ x_{An} & y_{An} & z_{An} \end{bmatrix} U_A=\begin{bmatrix} u_{A1} & v_{A1} & w_{A1} \\ \vdots & \vdots & \vdots \\ u_{An} & v_{An} & w_{An} \end{bmatrix}$$

The interpolation function coefficient equation based on structural node coordinates is:

$$A_S C = W_S \tag{2.16}$$

Where:

$$A=\begin{bmatrix} 0 & 0 & 0 & 0 & 1 & 1 & \cdots & 1 \\ 0 & 0 & 0 & 0 & x_{S1} & x_{S2} & \cdots & x_{Sn} \\ 0 & 0 & 0 & 0 & y_{S1} & y_{S2} & \cdots & y_{Sn} \\ 0 & 0 & 0 & 0 & z_{S1} & z_{S2} & \cdots & z_{Sn} \\ 1 & x_{S1} & y_{S1} & z_{S1} & h_1 & b_{12} & \cdots & b_{1n} \\ 1 & x_{S2} & y_{S2} & z_{S2} & b_{21} & h_2 & \cdots & b_{2n} \\ \vdots & \vdots & \vdots & \vdots & \vdots & \vdots & & \vdots \\ 1 & x_{Sn} & y_{Sn} & z_{Sn} & b_{n1} & b_{n2} & \cdots & h_n \end{bmatrix}$$

$$C=\begin{bmatrix} c_1^1 & c_1^2 & c_1^3 \\ c_2^1 & c_2^2 & c_2^3 \\ c_3^1 & c_3^2 & c_3^3 \\ c_4^1 & c_4^2 & c_4^3 \\ c_{4+1}^1 & c_{4+1}^2 & c_{4+1}^3 \\ c_{4+2}^1 & c_{4+2}^2 & c_{4+2}^3 \\ \vdots & \vdots & \vdots \\ c_{4+n}^1 & c_{4+n}^2 & c_{4+n}^3 \end{bmatrix} \quad W_S=\begin{bmatrix} 0 & 0 & 0 \\ 0 & 0 & 0 \\ 0 & 0 & 0 \\ 0 & 0 & 0 \\ u_{S1} & v_{S1} & w_{S1} \\ u_{S2} & v_{S2} & w_{S2} \\ \vdots & \vdots & \vdots \\ u_{Sn} & v_{Sn} & w_{Sn} \end{bmatrix}$$

$$h_i = 0, b_{ji} = r_{ji}^2 \ln\left(r_{ji}^2 + \varepsilon\right)$$

$$r_{ij}^2 = \left(x_{Sj} - x_{Si}\right)^2 + \left(y_{Sj} - y_{Si}\right)^2 + \left(z_{Sj} - z_{Si}\right)^2, \left(i, j = 1, 2, \cdots, n, i \neq j\right)$$

The displacement vector at the aerodynamic grid node can be expressed as:

$$U_A = A_A A_S^{-1} W_S = G U_S \tag{2.17}$$

Where G is the displacement interpolation matrix between structural nodes and aerodynamic nodes,

$$A_A = \begin{bmatrix} 1 & x_{S1} & y_{S1} & z_{S1} & h_1 & b_{12} & \cdots & b_{1n} \\ 1 & x_{S2} & y_{S2} & z_{S2} & b_{21} & h_2 & \cdots & b_{2n} \\ \vdots & \vdots & \vdots & \vdots & \vdots & \vdots & & \vdots \\ 1 & x_{Sn} & y_{Sn} & z_{Sn} & b_{n1} & b_{n2} & \cdots & h_n \end{bmatrix}$$

2.4 The force interpolation method

Another significant issue in aeroelastic analysis is to transfer the load information from the aerodynamic interface to the structural interface. This process is known as force interpolation. In aeroelastic analysis, force interpolation does not rely on principles like static equivalence or deformation equivalence commonly used in structural analysis. Instead, it adheres to the principle of structural equivalence, which ensures that two equivalent sets of loads have equal virtual work on any possible virtual displacement of the structure. If the virtual displacement of the structure is $\delta \mathbf{U}_S$, the virtual displacement of the aerodynamic interface is $\delta \mathbf{U}_A$, the load on the aerodynamic interface is $\mathbf{F}_A$, and the equivalent load on the structural interface is $\mathbf{F}_S$, then they satisfy the relationship:

$$\delta \mathbf{U}_A{}^T F_A = \delta \mathbf{U}_S{}^T \mathbf{F}_S \tag{2.18}$$

Where the interpolation relationship between the aerodynamic and structural interfaces' displacements is satisfied, i.e., $\delta \mathbf{U}_A = G \delta \mathbf{U}_S$, upon substitution into the equation considering the arbitrariness of virtual displacements, we obtain:

$$\mathbf{F}_S = G^T \mathbf{F}_A \tag{2.19}$$

2.5 Geometric Nonlinear Aeroelastic Analysis

Based on the above assumptions and principles, we can iteratively compute the deformation displacements for a given flight state. Utilizing the linearized modes corresponding to this state, we conduct flutter analysis. If the flutter results significantly deviate from the flight speed of this state, we need to reconsider the selection of the freestream velocity for nonlinear static aeroelastic computations and corresponding dynamic analyses near the equilibrium position. This process continues until the freestream velocity is relatively close to the flutter speed. The specific workflow is illustrated in Figure 3.

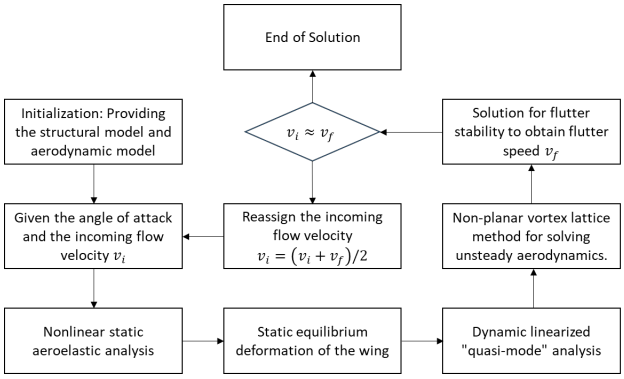

Figure 3. Curved surface dipole lattice division

3 REFERENCE MODEL

The simulation analysis in this study utilizes a large flexible wing model, as depicted in Figure 4. The wingspan of each individual flying unit is 1.96 meters, with a chord length of 0.1 meters. The mass of the wing structure is 1.187 kilograms. Detailed parameters refer to Table 1.

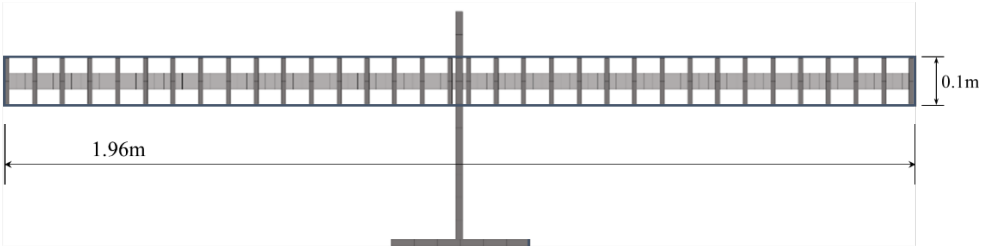

Figure 4. The structural model diagram of the individual aircraft.

Table 1 Structural Model Parameters

Parameters	Values	Parameters	Values
Span Length/ m	1.960	Position of Main Beam	50% Chord Length
Chord Length/ m	0.100	Modulus of Elasticity of Main Beam/ GPa	395.1
Structural mass/ kg	1.187	Cross-section Size of Main Beam/ m	0.035×0.0015

The composite flying vehicle model after connection is depicted in Figures 3 to 4. The connection adopts a hinge-type configuration, with a width set at 0.04 meters. Finite element modeling primarily employs RBE2 elements and spring elements for simulation purposes, and the spring elements are assigned a stiffness of 2000 N/m.

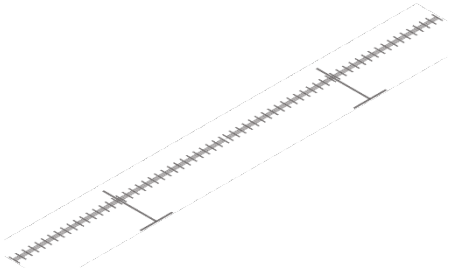

Figure 5. The structural model diagram of the two-body aircraft.

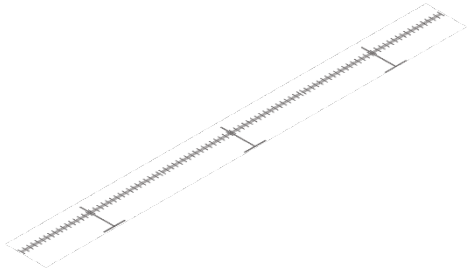

Figure 6. The structural model diagram of the three-body individual aircraft.

The results of the natural mode analysis for the individual flying unit are depicted in Figure 7. To enable free separation and combination in near-space environments, the individual flying unit itself belongs to the category of high aspect ratio flexible aircraft. This implies lower stiffness and elastic mode frequencies, suggesting significant deformation of the aircraft even when flying solo.

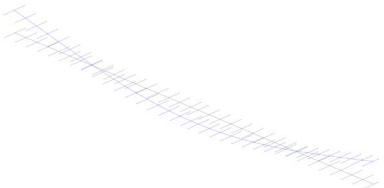

1st bending

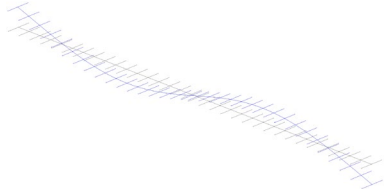

2nd bending

1st torsion 1st in-plane bending

Figure 7. Primary elastic modal shapes of single aircraft

The primary mode shapes of the composite unmanned aerial vehicle formed by the combination of two aircraft and three aircraft are illustrated in Figures 8-9. It is evident that the modal frequencies of the aircraft decrease significantly after combination, reaffirming the necessity of aeroelastic property analysis for this configuration. The main modal frequencies of each composite flying unit are listed in Table 2.

1st bending 2nd bending

1st in-plane bending 1st torsion

Figure 8. Primary elastic modal shapes of two-body aircraft

1st bending 2nd bending

1st in-plane bending 1st torsion

Figure 9. Primary elastic modal shapes of three-body aircraft

Table 2 Structural Model Parameters

Parameters	Single aircraft		2-body aircraft		3-body aircraft	
	Mode Order	Frequency (Hz)	Mode Order	Frequency (Hz)	Mode Order	Frequency (Hz)
1st bending	7	2.312	7	0.583	7	0.181
2nd bending	8	6.385	8	1.577	8	0.460
1st in-plane bending	14	53.86	13	13.600	14	5.993
1st torsion	13	46.57	17	23.441	19	15.630

4 AEROELASTICITY ANALYSIS OF MBA

4.1 The initial flow velocity obtained from linear aerodynamic-elastic analysis

The initial flow velocity v_i for iterative computation is determined through linear analysis. Taking the analysis process of a single aircraft as an example, a uniform grid of 60×6 cells is established along the spanwise and chordwise directions of the wing. The grid division of the aerodynamic surface of the wing is shown in Figure 10. To simplify the calculation, the grid division must remain consistent with the static aeroelastic analysis process.

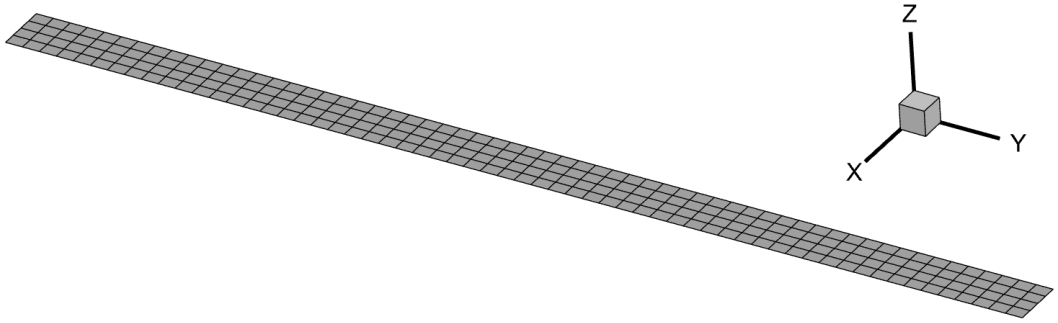

Figure 10 Aerodynamic Surface Model of the Single Aircraft Wing

The aerodynamic elastic model is obtained through interpolation between the aerodynamic surface model and the structural model. The initial flow velocity for the current state is taken as the flutter speed for that state. The interpolation results of the primary mode linear aerodynamic elastic model for the single aircraft, along with the flutter results, are illustrated in Figures 11-12. The flutter

speed is 38.120 m/s, with a flutter frequency of 13.976 Hz. The flutter mode exhibits coupling between the second-order bending mode and the first-order torsional mode.

1st bending 1st torsion

Figure 11. Interpolation results of the primary mode linear aerodynamic elastic model

v-g v-f

Figure 12. Linear flutter characteristics of single aircraft

The flutter results for the composite UAV obtained through the same initial flow value calculations are presented in Figure 13 and Table 3. The flutter modes observed in all cases exhibit a coupling flutter between the first-order torsional mode and a certain bending mode. From the linear calculation results, we can preliminarily infer that the flutter speed will decrease with an increase in the number of aircraft in the combination.

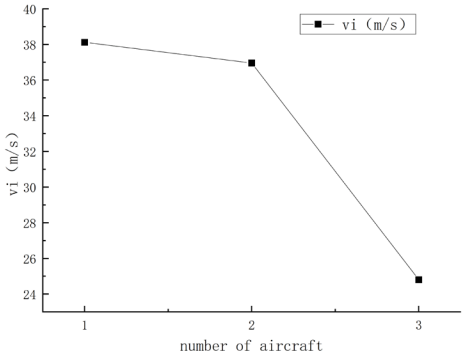

Figure 13. Flutter Speeds for Various Numbers of MBA

Table 3 Flutter characteristics for Various Numbers of MBA

Parameters	Flutter Speed (m/s)	Flutter Frequency (Hz)	Mode Order
Single aircraft	38.120	13.976	1st torsion (13th mode)
2-body aircraft	36.961	11.853	1st torsion (17th mode)
3-body aircraft	24.808	8.936	1st bending (7th mode)

4.2 Solving for the ‘quasi-modes’ at the static equilibrium position

At a 0.01° angle of attack and under the initial flow velocity conditions, the iterative convergence process of the vertical displacement of the wingtip is illustrated in Figure 14. In the initial calculation step, the wing is in its initial planar configuration, with no additional angle of attack induced by elastic deformation, resulting in relatively minor aerodynamic loads. However, in subsequent iterative calculations, the elastic angle of attack increases, and the effect of additional aerodynamic loads becomes significant. Consequently, both the vertical and spanwise displacements of the wing continuously increase until reaching convergence. Taking the single-aircraft scenario as an example, with the convergence condition set at 1 mm, the vertical displacement of the wing converges to 205.089 mm, approximately 10% of the wing's span.

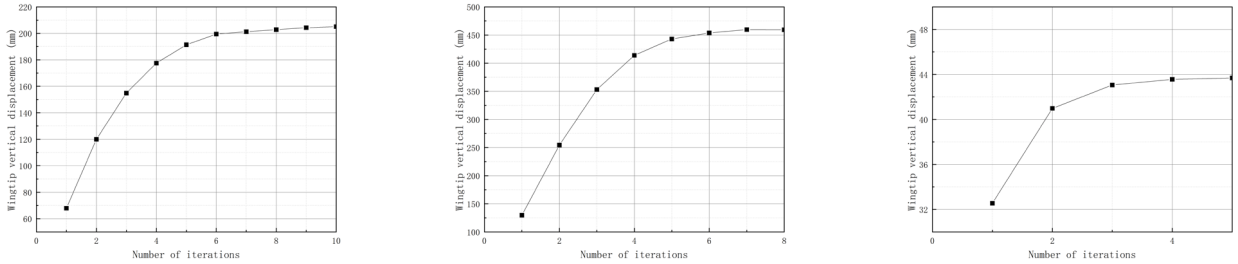

Single aircraft 2-body aircraft 3-body aircraft

Figure 14. Convergence process of vertical displacement

Figure 15 presents the computed results of the vertical displacements of the main beams for each configuration under this operating condition. For comparison, calculations are also performed using a nonlinear finite element-based static aeroelastic analysis method. The node displacements of the main beams computed by both methods exhibit minimal differences, indicating the rationality and accuracy of the static aeroelastic analysis method based on the nonlinear structural reduction model.

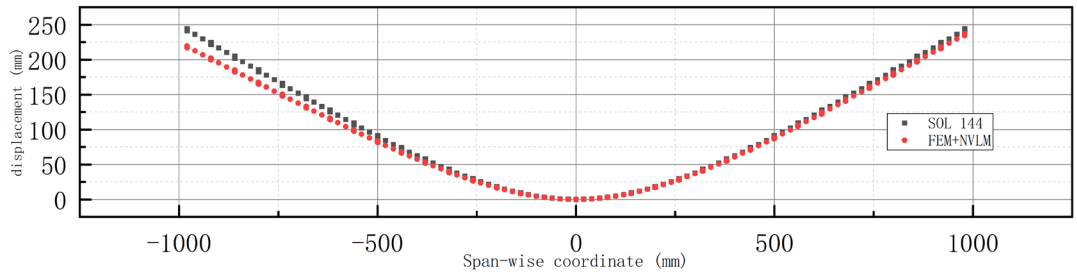

Single aircraft

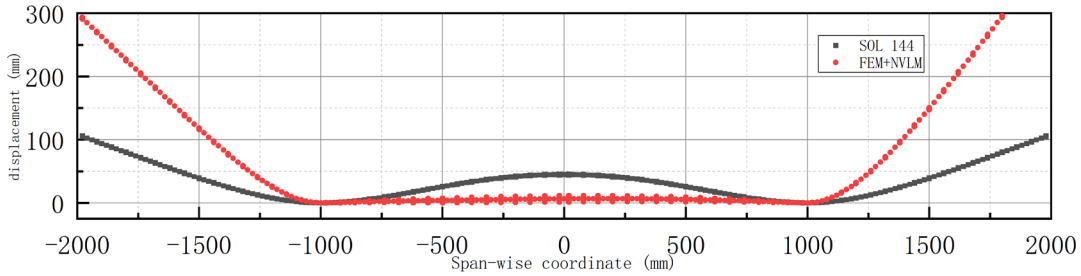

2-body aircraft

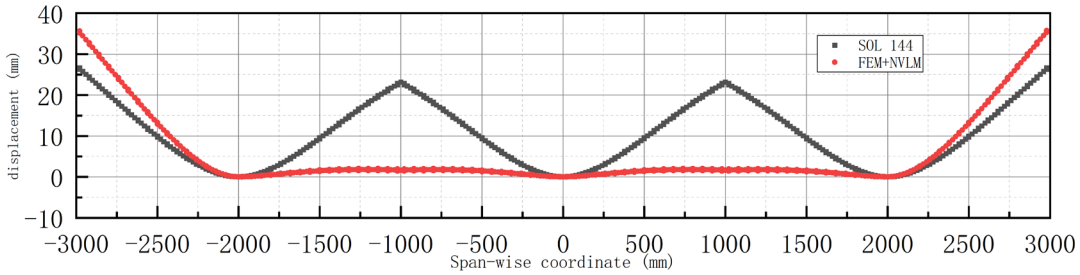

3-body aircraft

Figure 15. The vertical displacements of the main beams under static aeroelastic equilibrium

4.3 The initial flow velocity obtained from linear aerodynamic-elastic analysis

Under the initial flow velocity condition, linearized quasi-modes at static equilibrium positions for each configuration are obtained, as depicted in Figure 16. It can be observed that the form of linearized modes undergoes a noticeable transformation, with some linearized modes encompassing characteristics of other vibration modes. These factors contribute to the variability of nonlinear flutter characteristics with differing wing loading and deformation.

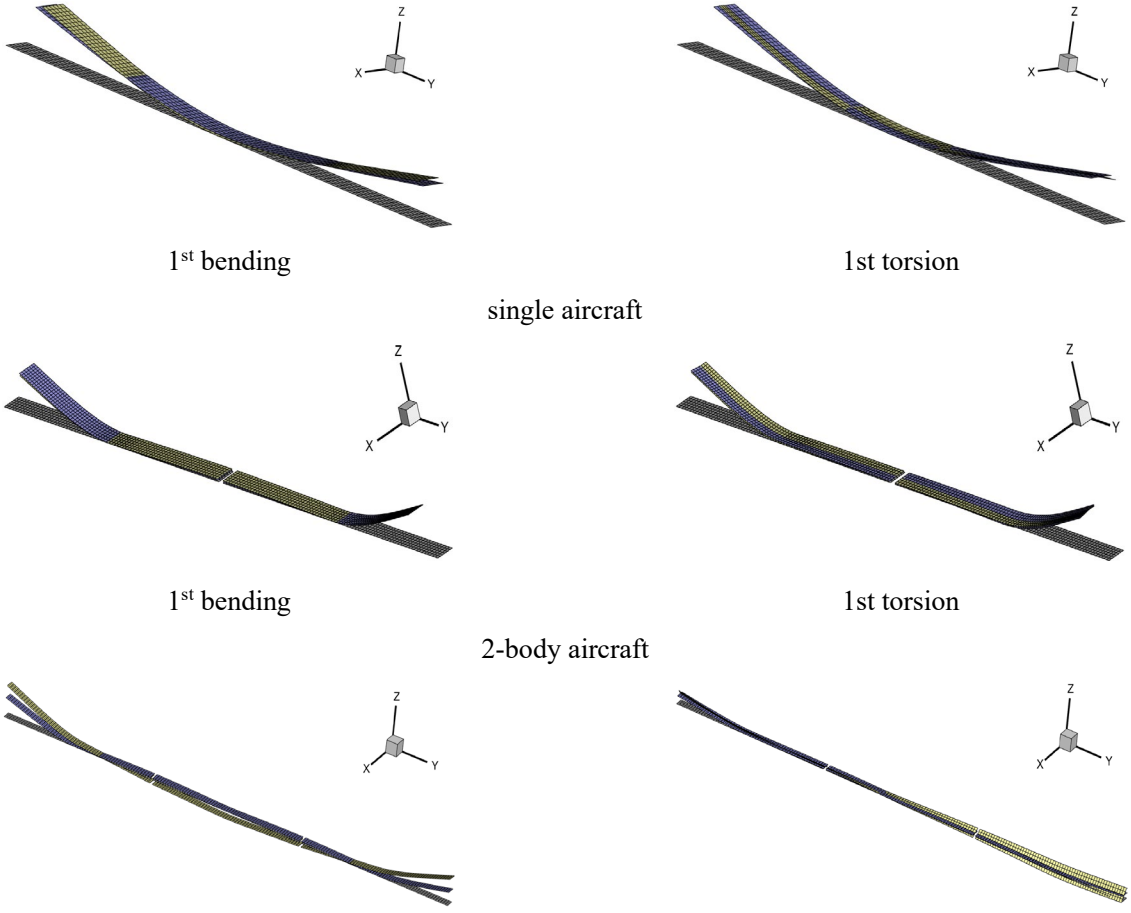

1st bending 1st torsion

single aircraft

1st bending 1st torsion

2-body aircraft

1st bending 1st torsion

3-body aircraft

Figure 16. Interpolation results of the primary mode linear aerodynamic elastic model

After multiple iterative calculations, the final flutter characteristics of each combined configuration at the static equilibrium state are determined, as shown in Figure 17 and Table 4. Compared to the linear calculation results, both the single aircraft and the combination of two aircraft occur flutter at lower speeds. This is because the static deformation state alters the original configuration of the aircraft, increasing its inherent flexibility. Additionally, some linearized modes contain other forms of vibrational characteristics, both factors contributing to the reduced flutter speed of the combined structure.

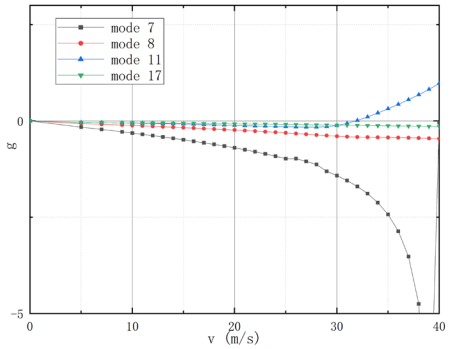

v-g

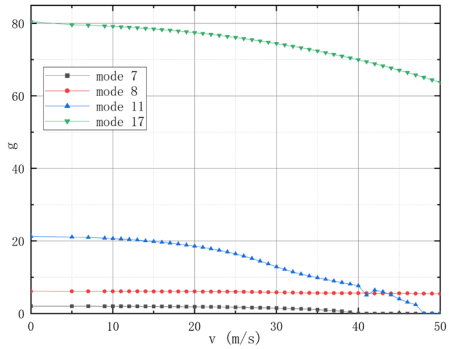

v-f

single aircraft

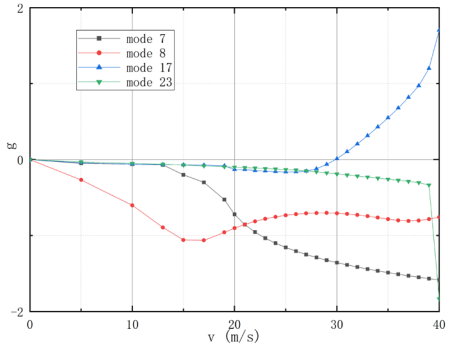

v-g

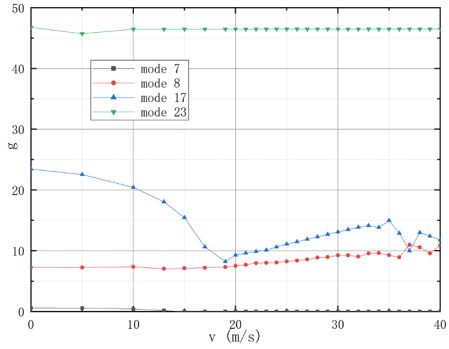

v-f

2-body aircraft

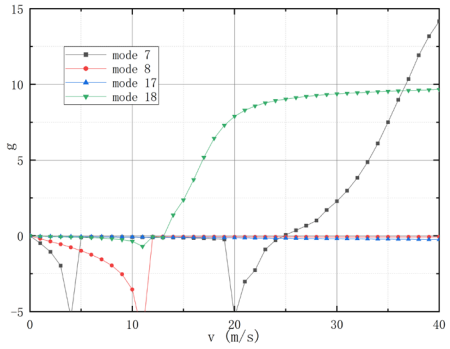

v-g

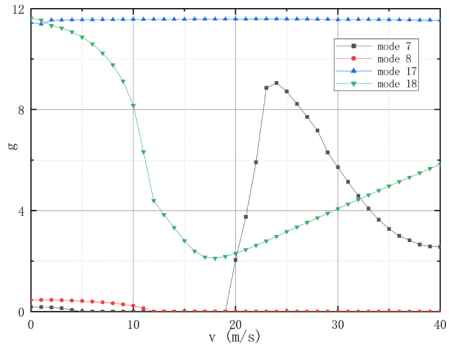

v-f

3-body aircraft

Figure 17. Nonlinear flutter characteristics

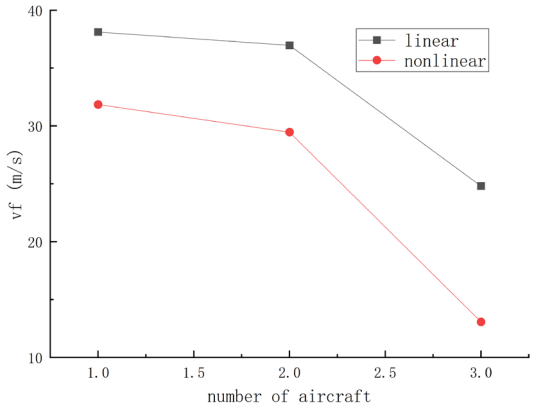

Figure 18. Flutter Speeds for Various Numbers of MBA

Table 4 Flutter characteristics for Various Numbers of MBA

Parameters	Flutter Speed (m/s)	Flutter Frequency (Hz)	Mode Order
Single aircraft	31.855	11.581	1st torsion (11th mode)
2-body aircraft	29.461	10.853	1st torsion (17th mode)
3-body aircraft	13.074	3.804	10st bending (18th mode)

5 CONCLUSIONS

To enhance the accuracy of flutter characteristics computation for composite configurations, we propose a quasi-modal modeling and analysis procedure integrating updated Lagrangian methodology and surface dipole grid method. This approach not only acknowledges the impact of nonlinear elements on aeroelastic property analysis but also circumvents the intricate solving process of high-dimensional nonlinear systems. Our findings indicate:

1. As the number of unmanned aircraft integrated into the composite increases, the composite's flexibility escalates, precipitating a substantial decrement in flutter speed. Notably, when three unmanned aircraft are amalgamated, the flutter speed dwindles to less than half of that of individual flying units. Hence, meticulous attention is warranted in composite configuration design to meet flutter-induced structural design prerequisites.

2. Comparative analysis with results obtained under linear conditions reveals a reduction in flutter speed upon considering geometric nonlinear factors. Across the three configurations scrutinized herein, flutter speed experiences an approximate 20% decrease. Consequently, geometric nonlinear elements must not be disregarded in the analysis of aeroelastic properties for composite configurations.

REFERENCES

[1] Knoedler A J. Lowering the high ground using near-space vehicles for persistent ISR[J]. Military Technology, 2008, 32(6): 178.

[2] Moomey E R. Technical Feasibility of Loitering Lighter-than-air-Near-space Maneuvering Vehicles[J]. 2005.

[3] Love M, Zink P, Wieselmann P, et al. Body freedom flutter of high aspect ratio flying wings[C]//46th AIAA/ASME/ASCE/AHS/ASC Structures, Structural Dynamics and Materials Conference. 2005: 1947.

[4] Wang X, Van Kampen E, Chu Q P, et al. Flexible aircraft gust load alleviation with incremental nonlinear dynamic inversion[J]. Journal of Guidance, Control, and Dynamics, 2019, 42(7): 1519-1536.

[5] Yang M, Chao A N, Changchuan X I E, et al. Conceptual design and flight test of two wingtip-docked multi-body aircraft[J]. Chinese Journal of Aeronautics, 2022, 35(12): 144-155.

[6] Magill S A. Compound aircraft transport study: Wingtip-docking compared to formation flight[D]. Virginia Polytechnic Institute and State University, 2002.

[7] Montalvo C. Meta aircraft flight dynamics and controls[D]. Georgia Institute of Technology, 2014.

[8] Patterson M D, Quinlan J, Fredericks W J, et al. A modular unmanned aerial system for missions requiring distributed aerial presence or payload delivery[C]//55th AIAA Aerospace Sciences Meeting. 2017: 0210.

[9] Montalvo C, Costello M. Meta aircraft connection dynamics[C]//AIAA Guidance, Navigation, and Control Conference. 2012: 4677.

[10] Montalvo C, Costello M. Meta aircraft flight dynamics[J]. Journal of Aircraft, 2015, 52(1): 107-115.

[11] Troub B, Montalvo C J. Meta aircraft controllability[C]//AIAA Atmospheric Flight Mechanics Conference. 2016: 3395.

[12] Cooper J R, Rothhaar P M. Dynamics and control of in-flight wing tip docking[J]. Journal of Guidance, Control, and Dynamics, 2018, 41(11): 2327-2337.

[13] Carithers C, Montalvo C. Experimental control of two connected fixed wing aircraft[J]. Aerospace, 2018, 5(4): 113.

[14] Cobar M, Montalvo C. Takeoff and landing of a wing-tip-connected meta aircraft with feedback control[J]. Journal of Aircraft, 2021, 58(4): 733-742.

[15] Chao A, Changchuan X, Yang M, et al. Flight mechanical analysis and test of unmanned multi-body aircraft[C]//International Forum on aeroelasticity and structural dynamics. 2019: 1-13.

[16] Yang M, Chao A N, Changchuan X I E, et al. Conceptual design and flight test of two wingtip-docked multi-body aircraft[J]. Chinese Journal of Aeronautics, 2022, 35(12): 144-155.

[17] Behrens A, Grund T, Ebert C, et al. Investigation of the aerodynamic interaction between two wings in a parallel flight with close lateral proximity[J]. CEAS Aeronautical Journal, 2020, 11: 553-563.

[18] Alexander K, Alexander B, Alexander H, et al. Closed-loop flight tests with an unmanned experimental multi-body aircraft[C]//17th international forum on aeroelasticity and structural dynamics, Como, Italy. 2017.

[19] Köthe A, Behrens A, Nowka D, et al. Transport delay in the distributed flight control system of an experimental multi-body aircraft with wireless communication[C]//Euro GNC–4th CEAS Specialist Conference on Guidance, Navigation & Control. 2017.

[20] Afonso F, Vale J, Oliveira É, et al. A review on non-linear aeroelasticity of high aspect-ratio wings[J]. Progress in Aerospace Sciences, 2017, 89: 40-57.

[21] Riso C, Cesnik C E. Low-Order Geometrically Nonlinear Aeroelastic Modeling and Analysis of the Pazy Wing Experiment[C]//AIAA SciTech 2022 Forum. 2022: 2313.

[22] Hilger J, Ritter M R. Nonlinear aeroelastic simulations and stability analysis of the pazy wing aeroelastic benchmark[J]. Aerospace, 2021, 8(10): 308.

[23] Hilger J, Ritter M. An Approach for Nonlinear Aeroelastic and Flight Dynamic Analyses for Very Flexible Aircraft at Trim States of Large Deformations[C]//AIAA SCITECH 2023 Forum. 2023: 0190.

[24] Xie C, An C, Liu Y, et al. Static aeroelastic analysis including geometric nonlinearities based on reduced order model[J]. Chinese Journal of Aeronautics, 2017, 30(2): 638-650.

COPYRIGHT STATEMENT